International Journal of Heat and Mass Transfer 110 (2017) 768–777

Contents lists available at ScienceDirect

International Journal of Heat and Mass Transfer

journal homepage: www.elsevier.com/locate/ijhmt

Steady state and transient analytical modeling of non-uniform convective cooling of a microprocessor chip due to jet impingement

S. Luhar, D. Sarkar, A. Jain *

Mechanical and Aerospace Engineering Department, University of Texas at Arlington, USA

ARTICLE INFO

Article history:
Received 23 December 2016
Received in revised form 10 February 2017
Accepted 17 March 2017

Keywords:
Jet impingement cooling
Thermal management
Thermal conduction
Convection
Analytical methods

ABSTRACT

Heat removal from microprocessor chips with multiple regions of dynamic heat generation remains a critical technological challenge. Excessive temperature rise is undesirable for performance as well as reliability. Jet impingement cooling has been widely investigated as a potential thermal management technique due to the capability of localized cooling and of dynamically following the heat generation distribution. A jet offers large local convective heat transfer coefficient, for which theoretical models and correlations have been proposed for a variety of scenarios. However, not much work exists on using this information to determine the resulting temperature distribution. This paper addresses this need by developing analytical steady state and transient heat transfer models that account for the spatial variation in convective heat transfer coefficient and for spatially non-uniform heat flux. The solution is derived in the form of an infinite series, the coefficients of which are determined by solving a set of algebraic equations. Temperature rise predicted by the models are found to be in excellent agreement with finite-element simulations, while offering faster computation time and easier integration with design and performance optimization tools used in microelectronics. The analytical model is used for predicting temperature rise in a variety of scenarios to examine interesting optimization problems such as the cooling of multiple hotspots with a single jet, determining the optimal location of a jet, etc. Results presented here may facilitate improved thermal design and real-time performance optimization of microprocessor chips.

© 2017 Elsevier Ltd. All rights reserved.

Overbars represent variables in Laplace domain.

1. Introduction

Cooling of a microprocessor chip is an important technological problem that has attracted significant research over past several decades [1–4]. Heat generated during transistor operation on a chip must be conducted through the chip and package, and rejected to the ambient in order to maintain the microprocessor temperature below an acceptable threshold. Thermal management directly affects device performance, as the mobility of charge carriers deteriorates at higher temperatures [5]. Device and package reliability is also adversely affected by high temperatures. Most modern microprocessor chips are multi-core in nature, and include several other power-intensive blocks such as Graphics Processing Units (GPUs) on the same substrate. This results in multiple regions of high power density, or hotspots, on the chip. Further, hotspots also shift dynamically, depending on the nature of microprocessor load, thereby presenting significant thermal management challenges. Specifically, it is difficult to reduce peak temperature rise on a hotspot using a passive thermal management technique that does not specifically address the hotspot location and the dynamic changes in power dissipation on the chip.

Natural convective cooling may be sufficient for very low power chips. At higher powers, air cooling is employed, typically by attaching a metal heat sink to the chip via a thermal interface material and heat spreader, and providing air flow over the heat sink [6]. Heat removal is also often carried out using a heat pipe or vapor chamber [7,8], particularly in space-constrained applications such as laptops. Single-phase and two-phase liquid cooling offer much larger heat transfer coefficients than air cooling. Much research has also been carried out for investigating liquid cooling for thermal management of higher-power chips [9]. These include liquid flow through microchannels, either in the heat sink, or on the back of the microprocessor chip itself, jet impingement on the chip backside [10], thin film liquid cooling utilizing electrowetting-on-discharge (EWOD) [11], etc. Both implementation and modeling of liquid-based cooling are more complicated than air cooling.

* Corresponding author at: 500 W First St, Rm 211, Arlington, TX 76019, USA.
E-mail address: jaina@uta.edu (A. Jain).

http://dx.doi.org/10.1016/j.ijheatmasstransfer.2017.03.064
0017-9310/© 2017 Elsevier Ltd. All rights reserved.

Nomenclature

a, b, c	dimensions
$A_{00}, B_{00}, A_{nm}, B_{nm}$	coefficients in the temperature field solution
C_{00}, C_{nm}	Fourier series coefficients for temperature field
C_p	heat capacity
d	jet diameter
h	convective heat transfer coefficient
k	thermal conductivity
N	norms
P_{00}, P_{nm}	Fourier series coefficients for heat flux field
q	heat flux
r	distance away from jet center
s	Laplace parameter
t	time
T	temperature rise
α	thermal diffusivity
γ	parameter representative of the width of the h vs r curve
λ	eigenvalue
ρ	density

Subscripts

max	maximum
min	minimum
x, y, z	rectilinear coordinates

A laminar liquid jet impinging on the backside of a chip offers very large local convective heat transfer coefficients in the vicinity of the impingement spot. This cooling approach offers several advantages such as spatially directed cooling, and rapid temporal response, and thus has been extensively studied. Key challenges in this approach include management of vapor formation due to boiling, laminar fluid delivery and exit, and dynamic hotspot management. Several papers have demonstrated the experimental implementation of this approach, often employing a chip with resistive heating and temperature sensors for mimicking an actual microprocessor chip. Synthetic air jets impinging on such a thermal test die have been shown to result in significant reduction in thermal resistance [12]. A method has been developed for three-dimensional visualization of single and multijet arrays using micron resolution particle image velocimetry [13]. Experiments have been carried out to study the effect of jet impingement of alumina–water based nanofluids for a range of physical parameters such as Reynolds number, Prandtl number and volume fraction [14]. Cu–water nanofluid jet array impingement has been reported to result in 6.8% heat transfer enhancement [15]. In comparison with a sizable literature on experimental investigation, there is relatively lesser work done on theoretical modeling of jet impingement based cooling of microprocessors.

A key parameter to consider in such a modeling effort is the spatial variation of convective heat transfer coefficient due to the impinging jet. Correlations for different shapes and flow conditions have been developed through experiments and theoretical modeling. Typically, the heat transfer coefficient is the highest in the vicinity of the impingement spot, and reduces farther away. A number of heat transfer regions have been identified, in which heat transfer correlations have been developed. Analytical development of correlations for local Nusselt number for single phase free surface circular liquid jets has been carried out [16]. By combining experimental results and theoretical solutions of jet impingement boundary layer, the impinging jet has been shown to hydrodynamically evolve through four distinct regions: stagnation zone, boundary layer, viscous similarity, developing turbulence and fully turbulent [17].

While such models help understand the fundamental nature of heat transfer in an impinging jet, such models have not been sufficiently translated into tools for predicting temperature distribution in the presence of an impinging jet. Modeling the spatial variation in convective heat transfer coefficient due to an impinging jet presents significant analytical difficulties that are not present when the heat transfer coefficient is uniform [18]. Some work exists where spatially varying convective heat transfer has been accounted for in fins [19], heat generating slab [20], cylinder [21] and sphere [22] using a variant of Fourier series expansion method, but there is a lack of such work for jet impingement cooling of microprocessors.

In this paper, a theoretical model is developed for predicting the steady-state and transient temperature distribution on a microprocessor chip in presence of spatially varying convective cooling due to jet impingement. A series solution is derived, and it is shown that the coefficients in this series can be determined by solving a set of coupled algebraic equations. The transient problem is solved by combining this approach with the Laplace transform technique. The resulting solutions are shown to agree well with finite-element simulation results. The models are used for analyzing the effect of jet cooling on thermal performance of microprocessor chips. Several interesting optimization problems, such as jet placement and jet fluid distribution are analyzed using the model, demonstrating the capability of rapid computation of temperature rise in a microprocessor with spatial and dynamic variation of convective cooling and heat generation.

2. Derivation of temperature distribution in steady state

Fig. 1 shows a schematic of the geometry of a microprocessor chip of dimensions $a \times b \times c$, with spatially and temporally varying heat flux on the bottom face and spatially varying convective heat transfer coefficient $h(x,y)$ on the top face due to impingement of one or multiple jets. The steady state problem is considered in this section. In general, thermal conductivity is assumed to be orthotropic. In this case, the governing energy equation for the temperature field is given by

$$k_x \frac{\partial^2 T}{\partial x^2} + k_y \frac{\partial^2 T}{\partial y^2} + k_z \frac{\partial^2 T}{\partial z^2} = 0 \tag{1}$$

The temperature field $T(x,y,z)$ satisfies the following boundary conditions given by

$$\frac{\partial T}{\partial x} = 0 \quad \text{at } x = 0, a \tag{2}$$

$$\frac{\partial T}{\partial y} = 0 \quad \text{at } y = 0, b \tag{3}$$

$$k_z \frac{\partial T}{\partial z} + q(x,y) = 0 \quad \text{at } z = 0 \tag{4}$$

$$k_z \frac{\partial T}{\partial z} + h(x,y) \cdot T = 0 \quad \text{at } z = c \tag{5}$$

In this case, the solution for the temperature field may be written as the following two-variable Fourier series [23,24]

$$T(x,y,z) = C_{00}(z) + \sum_{n=0}^{\infty} \sum_{m=0}^{\infty} C_{nm}(z) \cos\left(\frac{n\pi x}{a}\right) \cos\left(\frac{m\pi y}{b}\right) \tag{6}$$

Note that the double summation in Eq. (6) and subsequent equations in Sections 2 and 3 excludes the case where n and m are both

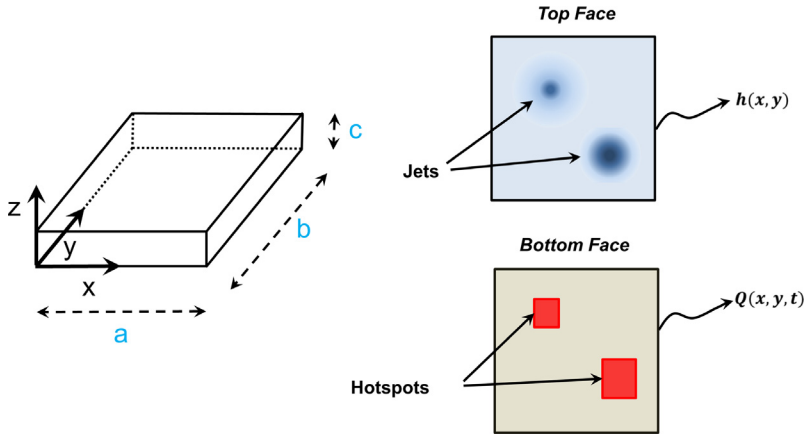

Fig. 1. Schematic of the geometry considered here for spatially varying convective cooling on the top face of a microprocessor chip with spatially varying heat generation on the bottom face.

zero, since that term is being considered separately. Eq. (6) satisfies Eqs. (2) and (3). Functions $C_{00}(z)$ and $C_{nm}(z)$ must be chosen so as to satisfy the remaining equations. To proceed, the given heat flux distribution $q(x,y)$ is expressed as a Fourier cosine series in two variables

$$q(x,y) = P_{00} + \sum_{n=0}^{\infty}\sum_{m=0}^{\infty} P_{nm} \cos\left(\frac{n\pi x}{a}\right) \cos\left(\frac{m\pi y}{b}\right) \tag{7}$$

where

$$P_{00} = \int_0^b \int_0^a q(x,y)\, dxdy \tag{8}$$

$$P_{nm} = \frac{\delta_{nm}}{ab} \int_0^b \int_0^a q(x,y) \cos\left(\frac{m\pi y}{b}\right) \cos\left(\frac{n\pi x}{a}\right) dx\, dy \tag{9}$$

$$\delta_{\mathrm{nm}} = \begin{cases} 4 & n\neq 0,\ m\neq 0 \\ 2 & otherwise \end{cases} \tag{10}$$

Substituting Eq. (6) in Eq. (1) results in

$$C''_{00}(z) + \sum_{m=0}^{\infty}\sum_{n=0}^{\infty} \cos\left(\frac{n\pi x}{a}\right) \cos\left(\frac{m\pi y}{b}\right) \left[C''_{nm}(z) - \tilde{k}_x \left(\frac{n\pi}{a}\right)^2 C_{nm}(z) - \tilde{k}_y \left(\frac{m\pi}{b}\right)^2 C_{nm}(z)\right] = 0 \tag{11}$$

Here, $\tilde{k}_x = \frac{k_x}{k_z}$ and $\tilde{k}_y = \frac{k_y}{k_z}$ are the thermal conductivity ratios that account for orthotropy in thermal conductivity, if present.

As a result, $C_{00}(z)$ and $C_{nm}(z)$ may be written as

$$C_{00}(z) = A_{00} + B_{00} z \tag{12}$$

$$C_{nm}(z) = A_{nm} \exp(\lambda_{nm} z) + B_{nm} \exp(-\lambda_{nm} z) \tag{13}$$

where $\lambda_{nm}^2 = \tilde{k}_x \left(\frac{n\pi}{a}\right)^2 + \tilde{k}_y \left(\frac{m\pi}{b}\right)^2$.

Using the boundary condition at $z = 0$, Eqs. (12) and (13) may be simplified to

$$C_{00}(z) = A_{00} - \frac{P_{00}}{k_z} z \tag{14}$$

$$C_{nm}(z) = A_{nm}(\exp(\lambda_{nm} z) + \exp(-\lambda_{nm} z)) + \frac{P_{nm}}{\lambda_{nm} k_z} \exp(-\lambda_{nm} z) \tag{15}$$

These expressions involve several unknowns – A_{00} and A_{nm} – which may be obtained using the boundary conditions at $z = c$. Substituting Eqs. (14) and (15) in (5) results in

$$\begin{aligned} &A_{00} h(x,y) + \sum_{n=0}^{\infty}\sum_{m=0}^{\infty} A_{nm} k_z \lambda_{nm} (\exp(\lambda_{nm} c) - \exp(-\lambda_{nm} c)) \cos\left(\tfrac{n\pi x}{a}\right) \cos\left(\tfrac{m\pi y}{b}\right) \\ &+ \sum_{n=0}^{\infty}\sum_{m=0}^{\infty} A_{nm} (\exp(\lambda_{nm} c) + \exp(-\lambda_{nm} c)) h(x,y) \cos\left(\tfrac{n\pi x}{a}\right) \cos\left(\tfrac{m\pi y}{b}\right) \\ &= P_{00}\left(1 + \tfrac{ch(x,y)}{k_z}\right) + \sum_{n=0}^{\infty}\sum_{m=0}^{\infty} P_{nm}\left(1 - \tfrac{h(x,y)}{\lambda_{nm} k_z}\right) \exp(-\lambda_{nm} c) \cos\left(\tfrac{n\pi x}{a}\right) \cos\left(\tfrac{m\pi y}{b}\right) \end{aligned} \tag{16}$$

While the summations in Eq. (16) go up to infinity, for computation, the upper limit is taken to be n = N and m = M. In order to extract the unknowns A_{00} and A_{nm}, Eq. (16) is integrated in x and y, resulting in a linear algebraic equation involving the unknown coefficients

$$\begin{aligned} &A_{00} \textstyle\int_0^b \int_0^a h(x,y) dxdy \\ &+ \sum_{n=0}^{N}\sum_{m=0}^{M} A_{nm} (\exp(\lambda_{nm} c) + \exp(-\lambda_{nm} c)) \textstyle\int_0^b \int_0^a h(x,y) \cos\left(\tfrac{n\pi x}{a}\right) \cos\left(\tfrac{m\pi y}{b}\right) dxdy \\ &= P_{00} ab + P_{00} \tfrac{c}{k_z} \textstyle\int_0^b \int_0^a h(x,y) dxdy \\ &- \sum_{n=0}^{N}\sum_{m=0}^{M} \tfrac{P_{nm}}{k_z \lambda_{nm}} \exp(-\lambda_{nm} c) \textstyle\int_0^b \int_0^a h(x,y) \cos\left(\tfrac{n\pi x}{a}\right) \cos\left(\tfrac{m\pi y}{b}\right) dxdy \end{aligned} \tag{17}$$

Also, Eq. (16) is multiplied by $\cos\left(\frac{i\pi x}{a}\right) \cos\left(\frac{j\pi y}{b}\right)$ for $i = 0,1,2,\ldots,N$ and $j = 0,1,2,\ldots,M$, except when i and j are both zero, and then integrated in x and y. Several terms drop out due to orthogonality of the eigenfunctions. For each i and j,

$$A_{00} f_{ij} + A_{ij} e_{ij} + \sum_{n=0}^{N}\sum_{m=0}^{M} A_{nm} d_{ijnm} = P_{00} u_{ij} + P_{ij} v_{ij} + \sum_{n=0}^{N}\sum_{m=0}^{M} P_{nm} w_{ijnm} \tag{18}$$

where the various terms are given by

$$f_{ij} = \int_0^a \int_0^b h(x,y) \cos\left(\frac{i\pi x}{a}\right) \cos\left(\frac{j\pi y}{b}\right) dx\, dy \tag{19}$$

$$e_{ij} = k_z \lambda_{ij} (\exp(\lambda_{ij} c) - \exp(-\lambda_{ij} c)) N_{x,i} N_{y,j} \tag{20}$$

$$d_{ijnm} = (\exp(\lambda_{nm} c) + \exp(-\lambda_{nm} c)) \int_0^a \int_0^b h(x,y) \cos\left(\frac{i\pi x}{a}\right) \times \cos\left(\frac{j\pi y}{b}\right) \cos\left(\frac{n\pi x}{a}\right) \cos\left(\frac{m\pi y}{b}\right) dxdy \tag{21}$$

$$u_{ij} = \frac{c}{k_z} f_{ij} \tag{22}$$

$$v_{ij} = \frac{\exp(-\lambda_{ij}c)}{k_z\,\lambda_{ij}\,(\exp(\lambda_{ij}c) - \exp(-\lambda_{ij}c))}\, e_{ij} \tag{23}$$

$$w_{ijnm} = \frac{-\exp(-\lambda_{nm}c)}{k_z \lambda_{nm}(\exp(\lambda_{nm}c) + \exp(-\lambda_{nm}c))}\, d_{ijnm} \tag{24}$$

The norms $N_{x,i}$ and $N_{y,j}$ in Eq. (20) are given by [25]

$$N_{x,i} = \int_0^a \cos^2\left(\frac{i\pi x}{a}\right) dx = \begin{cases} a & i = 0 \\ a/2 & \text{otherwise} \end{cases} \tag{25}$$

$$N_{y,j} = \int_0^b \cos^2\left(\frac{j\pi y}{b}\right) dy = \begin{cases} b & j = 0 \\ b/2 & \text{otherwise} \end{cases} \tag{26}$$

Eqs. (17) and (18) represent a set of $(N+1)\times(M+1)$ equations in $(N+1)\times(M+1)$ variables, which can be solved using matrix inversion to complete the solution for the steady-state temperature field.

3. Derivation of transient temperature distribution

The governing transient energy equation is similar to Eq. (1), and includes a transient term as follows:

$$k_x \frac{\partial^2 T}{\partial x^2} + k_y \frac{\partial^2 T}{\partial y^2} + k_z \frac{\partial^2 T}{\partial z^2} = \rho c_p \frac{\partial T}{\partial t} \tag{27}$$

subject to boundary conditions given by Eqs. (2), (3) and (5). There is a small change in the boundary condition at $z = 0$ to account for the transient variation in heat flux

$$k_z \frac{\partial T}{\partial z} + q(x,y,t) = 0 \quad \text{at } z = 0 \tag{28}$$

In addition, zero temperature rise is assumed at the initial time.

$$T = 0 \quad \text{at } t = 0 \tag{29}$$

The Laplace transform method is used to solve for the transient temperature field. Laplace transform of Eq. (27) results in

$$\tilde{k}_x \frac{\partial^2 \bar{T}}{\partial x^2} + \tilde{k}_y \frac{\partial^2 \bar{T}}{\partial y^2} + \frac{\partial^2 \bar{T}}{\partial z^2} = \frac{s}{\alpha_z} \bar{T} \tag{30}$$

where $\tilde{k}_x = \frac{k_x}{k_z}$, $\tilde{k}_y = \frac{k_y}{k_z}$ and $\alpha_z = \frac{k_z}{\rho c_p}$ is the thermal diffusivity using thermal conductivity in the z direction.

The boundary conditions are transformed to

$$\left.\frac{\partial \bar{T}}{\partial x}\right|_{x=0,a} = 0 \tag{31}$$

$$\left.\frac{\partial \bar{T}}{\partial y}\right|_{y=0,b} = 0 \tag{32}$$

$$k_z \left.\frac{\partial \bar{T}}{\partial z}\right|_{z=0} + \bar{q}(x,y,s) = 0 \tag{33}$$

$$k_z \frac{\partial \bar{T}}{\partial z} + h(x,y)\cdot \bar{T} = 0 \quad \text{at } z = c \tag{34}$$

$\bar{q}(x,y,s)$ in Eq. (33) is the Laplace transform of the applied heat flux$q(x,y,t)$.

The transient temperature distribution is determined using a similar approach as Section 2. $\bar{q}(x,y,s)$ is first expanded as follows

$$\bar{q}(x,y,s) = \bar{P}_{00}(s) + \sum_{n=0}^{\infty}\sum_{m=0}^{\infty} \bar{P}_{nm}(s) \cos\left(\frac{n\pi x}{a}\right) \cos\left(\frac{m\pi y}{b}\right) \tag{35}$$

where the coefficients $\bar{P}_{00}(s)$ and $\bar{P}_{nm}(s)$ are found similar to the coefficients P_{00} and P_{nm} in Section 2.

$$\bar{P}_{00}(s) = \int_0^a \int_0^b \bar{q}(x,y,s)\, dy\, dx \tag{36}$$

$$\bar{P}_{nm}(s) = \frac{\delta_{nm}}{ab} \int_0^a \int_0^b \bar{q}(x,y,s) \cos\left(\frac{m\pi y}{b}\right) \cos\left(\frac{n\pi x}{a}\right) dy\, dx \tag{37}$$

The temperature solution is given by

$$\bar{T}(x,y,z,s) = \bar{C}_{00}(z,s) + \sum_{n=0}^{\infty}\sum_{m=0}^{\infty} \bar{C}_{nm}(z,s) \cos\left(\frac{n\pi x}{a}\right) \cos\left(\frac{m\pi y}{b}\right) \tag{38}$$

where, using the governing energy equation and the boundary condition at $z = 0$, it is found that

$$\bar{C}_{00}(z,s) = \bar{A}_{00}\left(e^{\sqrt{\frac{s}{\alpha_z}}z} + e^{-\sqrt{\frac{s}{\alpha_z}}z}\right) + \frac{\bar{P}_{00}(s)}{k_z\sqrt{\frac{s}{\alpha_z}}} e^{-\sqrt{\frac{s}{\alpha_z}}z} \tag{39}$$

$$\bar{C}_{nm}(z,s) = \bar{A}_{nm}\left(e^{\bar{\lambda}_{nm}z} + e^{-\bar{\lambda}_{nm}z}\right) + \frac{\bar{P}_{nm}(s)}{k_z\,\bar{\lambda}_{nm}} e^{-\bar{\lambda}_{nm}z} \tag{40}$$

Here, the eigenvalues $\bar{\lambda}_{nm}$ are given by

$$\bar{\lambda}_{nm}^2 = \tilde{k}_x\left(\frac{n\pi}{a}\right)^2 + \tilde{k}_y\left(\frac{m\pi}{b}\right)^2 + \frac{s}{\alpha_z} \tag{41}$$

Substituting Eq. (38) in Eq. (34) results in

$$\begin{aligned}
&A_{00}\left\{k_z\sqrt{\tfrac{s}{\alpha_z}}\left(e^{\sqrt{\frac{s}{\alpha_z}}c} - e^{-\sqrt{\frac{s}{\alpha_z}}c}\right) + \left(e^{\sqrt{\frac{s}{\alpha_z}}c} + e^{-\sqrt{\frac{s}{\alpha_z}}c}\right)h(x,y)\right\} \\
&+\sum_{n=0}^{\infty}\sum_{m=0}^{\infty} A_{nm}\left\{\begin{array}{l} k_z\,\bar{\lambda}_{nm}(e^{\bar{\lambda}_{nm}c} - e^{-\bar{\lambda}_{nm}c}) \\ +(e^{\bar{\lambda}_{nm}c} + e^{-\bar{\lambda}_{nm}c})h(x,y)\end{array}\right\} \cos\left(\tfrac{n\pi x}{a}\right)\cos\left(\tfrac{m\pi y}{b}\right) \\
&= \bar{P}_{00}(s)\left\{e^{-\sqrt{\frac{s}{\alpha_z}}c} - \frac{1}{k_z\sqrt{s/\alpha_z}} e^{-\sqrt{\frac{s}{\alpha_z}}c} h(x,y)\right\} \\
&+\sum_{n=0}^{\infty}\sum_{m=0}^{\infty} \bar{P}_{nm}(s)\left\{1 - \frac{1}{k_z\,\bar{\lambda}_{nm}}\right\} e^{-\bar{\lambda}_{nm}c} h(x,y) \cos\left(\tfrac{n\pi x}{a}\right)\cos\left(\tfrac{m\pi y}{b}\right)
\end{aligned} \tag{42}$$

Similar to Section 2, consideration up to n = N and m = M terms, and integration of Eq. (42) in x and y results in

$$\begin{aligned}
&-\bar{A}_{00}k_z\sqrt{\tfrac{s}{\alpha_z}}\left(e^{\sqrt{\frac{s}{\alpha_z}}c} - e^{-\sqrt{\frac{s}{\alpha_z}}c}\right)\cdot a\cdot b - \bar{A}_{00}\left(e^{\sqrt{\frac{s}{\alpha_z}}c} + e^{-\sqrt{\frac{s}{\alpha_z}}c}\right)\int_0^b\int_0^a h(x,y)dxdy \\
&-\sum_{n=0}^{N}\sum_{m=0}^{M} \bar{A}_{nm}(e^{\bar{\lambda}_{nm}c} + e^{-\bar{\lambda}_{nm}c})\int_0^b\int_0^a h(x,y)\cos\left(\tfrac{n\pi x}{a}\right)\cos\left(\tfrac{m\pi y}{b}\right)dxdy \\
&= -\bar{P}_{00}(s)e^{-\sqrt{\frac{s}{\alpha_z}}c}ab + \frac{\bar{P}_{00}(s)}{k_z\sqrt{s/\alpha_z}} e^{-\sqrt{\frac{s}{\alpha_z}}c}\int_0^b\int_0^a h(x,y)dxdy \\
&+\sum_{n=0}^{N}\sum_{m=0}^{M} \frac{\bar{P}_{nm}(s)}{k_z\,\bar{\lambda}_{nm}} e^{-\bar{\lambda}_{nm}c}\int_0^b\int_0^a h(x,y)\cos\left(\tfrac{n\pi x}{a}\right)\cos\left(\tfrac{m\pi y}{b}\right)dxdy
\end{aligned} \tag{43}$$

Also, Eq. (42) is multiplied by $\cos\left(\frac{i\pi x}{a}\right)\cos\left(\frac{j\pi y}{b}\right)$ for $i = 0,1,2,\ldots,N$ and $j = 0,1,2,\ldots,M$, except when i and j are both zero, and then integrated in x and y. Simplification using principle of orthogonality similar to Section 2 results in

$$\bar{A}_{00}\bar{f}_{ij} + \bar{A}_{ij}\bar{e}_{ij} + \sum_{n=0}^{N}\sum_{m=0}^{M} \bar{A}_{nm}\bar{d}_{ijnm} = \bar{P}_{00}(s)\bar{u}_{ij} + \bar{P}(s)_{ij}\bar{v}_{ij} + \sum_{n=0}^{N}\sum_{m=0}^{M} \bar{P}_{nm}\bar{w}_{ijnm} \tag{44}$$

where the various terms are given by

$$\bar{f}_{ij} = \left(e^{\sqrt{\frac{s}{\alpha_z}}c} + e^{-\sqrt{\frac{s}{\alpha_z}}c}\right)\int_0^a\int_0^b h(x,y)\cos\left(\frac{i\pi x}{a}\right)\cos\left(\frac{j\pi y}{b}\right)dxdy \tag{45}$$

$$\bar{e}_{ij} = k_z\bar{\lambda}_{ij}(e^{\bar{\lambda}_{ij}c} - e^{-\bar{\lambda}_{ij}c})N_{x,i}N_{y,j} \tag{46}$$

$$\bar{d}_{ijnm} = \left(e^{\bar{\lambda}_{nm}c} + e^{-\bar{\lambda}_{nm}c}\right) \int_0^a \int_0^b h(x,y) \times \cos\left(\frac{i\pi x}{a}\right) \cos\left(\frac{j\pi y}{b}\right) \cos\left(\frac{n\pi x}{a}\right) \cos\left(\frac{m\pi y}{b}\right) dxdy \quad (47)$$

$$\bar{u}_{ij} = \frac{-e^{-\sqrt{\frac{s}{\alpha_z}}c}}{k_z\sqrt{\frac{s}{\alpha_z}}\left(e^{\sqrt{\frac{s}{\alpha_z}}c} + e^{-\sqrt{\frac{s}{\alpha_z}}c}\right)}\bar{f}_{ij} \quad (48)$$

$$\bar{v}_{ij} = \frac{e^{-\bar{\lambda}_{ij}c}}{k_z\,\bar{\lambda}_{ij}\left(e^{\bar{\lambda}_{ij}c} - e^{-\bar{\lambda}_{ij}c}\right)}\bar{e}_{ij} \quad (49)$$

$$\bar{w}_{ijnm} = \frac{-e^{-\bar{\lambda}_{nm}c}}{k_z\,\bar{\lambda}_{nm}\left(e^{\bar{\lambda}_{nm}c} + e^{-\bar{\lambda}_{nm}c}\right)}\bar{d}_{ijnm} \quad (50)$$

This set of linear algebraic equations can be solved using matrix inversion similar to Section 2. The solution for the temperature distribution in the Laplace domain represented by Eq. (38) must be inverted for the final solution. Due to the complicated nature of the solution, Laplace inversion is carried out using the de Hoog's quotient difference method algorithm [26] as implemented by Hollenbeck [27].

4. Results and discussion

The impingement of a cooling jet on a surface produces a spatially varying convective heat transfer coefficient. While the precise nature of the convective heat transfer coefficient depends on a number of parameters related to the fluid flow in the jet [17], such as turbulence, convective heat transfer due to an impinging jet is often modeled using representative functions that produce large values of the convective heat transfer coefficient in and close to the jet region, and decline to lower values farther out. In this work, in order to demonstrate the capability of the analytical model to compute the temperature distribution for spatially varying convective heat transfer, the following expression is used for $h(r)$ based on past work [20]:

$$h(r) = h_{\max}\left[\frac{1 - R\tanh\left(\gamma\left(\frac{r}{d} - \frac{3}{2}\right)\right)}{1+R}\right] \quad (51)$$

where r is the distance away from the jet center and $R = \frac{h_{\max} - h_{\min}}{h_{\max} + h_{\min}}$. In this definition, d refers to the jet diameter, and h_{max} and h_{min} refer to the convective heat transfer coefficient at the jet impingement location and far away from the jet respectively. The parameter γ is representative of the width of the h vs r curve.

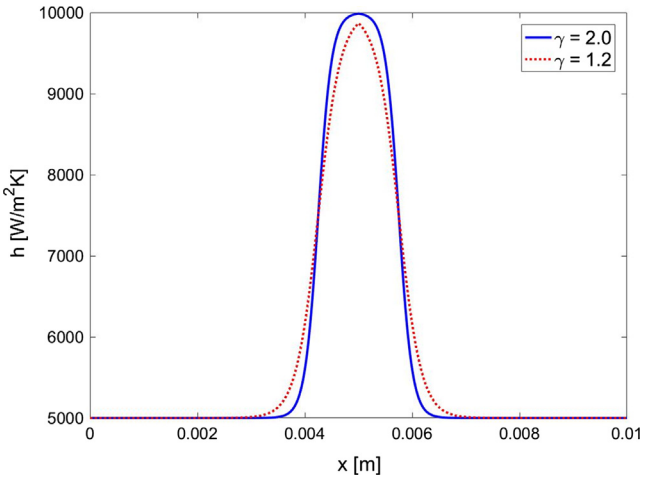

Fig. 2. Convective heat transfer coefficient as a function of radial distance from the jet center based on Eq. (51).

Fig. 2 plots h as a function of r for two values of γ, showing that the value of γ can be used to modulate the region of influence of the impinging jet. In general, the lower the value of γ, the larger is the region of influence due to the jet. While the purpose of the present work is not to analyze convective heat transfer due to an impinging jet, Eq. (51) provides a convenient model for convective heat transfer coefficients for jet impingement with which to study the analytical models in Sections 2 and 3 for predicting steady state and transient temperature rise due to the spatially varying convective heat transfer.

Although the models are derived assuming orthotropic thermal conductivity, the rest of the paper assumes a constant thermal conductivity in all directions, as is usual for Silicon and other commonly used materials for substrates of microelectronic chips. The analytical model described in Sections 2 and 3 are validated by comparison with finite-element simulations. Finite-element simulations are carried out in a commercial software in which the geometry of the microprocessor chip, including the desired power map is modeled and meshed with around 750000 elements. Power dissipation is modeled as a heat flux boundary condition on one face, whereas jet cooling is modeled with a spatially varying convective heat transfer coefficient on the other face. Grid-independence of the finite-element simulation is ensured. The finite-element simulation serves to provide a validation of the analytical model.

Fig. 3 presents a comparison for a steady-state case, with two hotspots of sizes 1 mm by 1 mm, each generating 10 W/mm^2 heat in a 10 mm $\times$ 10 mm microprocessor die, which is being cooled by a single jet impinging on the other side of the die at the location corresponding to the first hotspot. The convective heat transfer parameters of the impinging jet are h_{max} = 60000 W/m^2 K, h_{min} = 5000 W/m^2 K, γ = 2, and d = 0.5 mm. Colorplots for the analytical model and finite-element simulation results shown in Fig. 3(a) indicate very close agreement between the two, less than 4.8% over the entire microprocessor die. The close agreement between the two is further illustrated in Fig. 3(b), which show the variation of temperature along two lines passing through the centers of the two hotspots.

The typical computation time for computing temperature at a point of interest using the analytical model is around 5 s, compared to 1–2 min for the finite-element simulation depending on the level of convergence desired. Note that this is in addition to time taken for setting up the geometry and creating a mesh for the simulation. A further computational advantage is observed for transient cases, where the finite-element simulation takes much longer due to the need for timestepping and convergence at each time step.

In order to validate the transient model presented in Section 3, a computation is carried out to predict temperature as a function of time for a two-hotspot case, where the first hotspot remains on between t = 0 s and t = 0.1 s, and the second hotspot stays on afterwards. For ease of computation, a two-dimensional geometry is considered for transient computations. Fig. 4(a) compares the computed temperature at the center of the chip as a function of time with finite-element simulations. The two are found to be in very good agreement through the computation period, with a worst-case deviation of less than 2.4%. Fig. 4(b) plots the temperature as a function of x at t = 0.25 s, at which the first hotspot of size 1 mm and centered at 2.5 mm has switched off while the second hotspot of the same size and centered at x = 7.5 mm is active. As expected, the peak temperature occurs at the second hotspot, and there is very good agreement between analytical computations and finite-element simulation results, with a worst-case deviation of less than 1.6%.

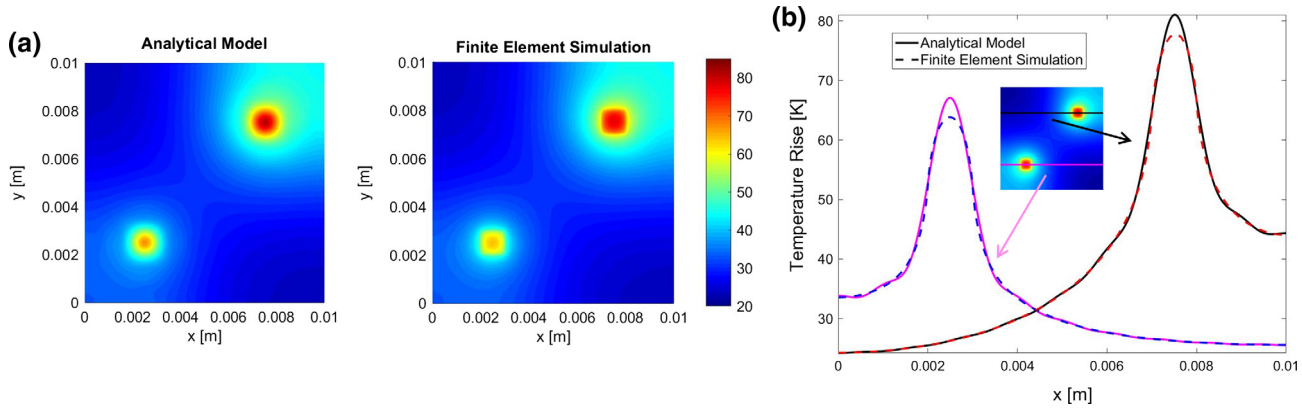

Fig. 3. Comparison of the steady-state analytical model results with finite-element simulations for a microprocessor chip with two hotspots and a single cooling jet at the center of one of the hotspots. (a) shows the full colorplot, while (b) shows the temperature as function of x along two lines.

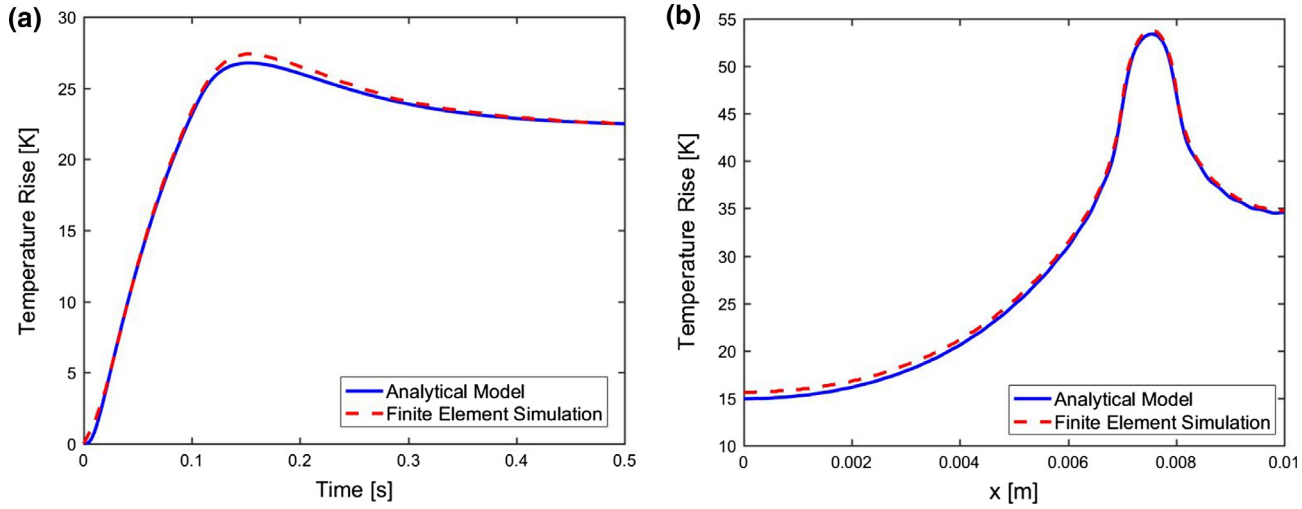

Fig. 4. Comparison of the transient analytical model with finite-element simulations for a two-hotspot case where both are active during different time intervals. (a) shows temperature as a function of time at the center of the chip, while (b) shows temperature rise as a function of x at t = 0.25 s.

The close agreement of temperature computed using the models presented in Sections 2 and 3 with finite-element simulation results provide validation of these analytical models. In comparison with finite-element simulations, these models offer faster computational time. The analytical nature of the solution also offers greater ease of integration with other computations related to the microprocessor chip, which might make it possible to predict and monitor the temperature of the chip in real time. Finally, the analytical solution enables parametric study of the effect of various parameters on the temperature field on the chip, which is cumbersome and time-consuming to perform through finite-element simulations.

Since the analytical solution for temperature is obtained in terms of an infinite series, the coefficients of which must be determined by solving a set of coupled algebraic equations, it is important to determine the minimum number of eigenvalues required to ensure reasonable accuracy of the analytical model. In general, the larger the number of eigenvalues, the larger is the set of algebraic equations such as Eq. (18) and thus the greater is the computational effort. Fig. 5 plots the computed temperature as a function of space with varying numbers of eigenvalues in each spatial direction. For comparison, results from a finite-element simulation are also shown. Fig. 5 shows convergence of the computed temperature distribution towards the finite-element simulation curve as

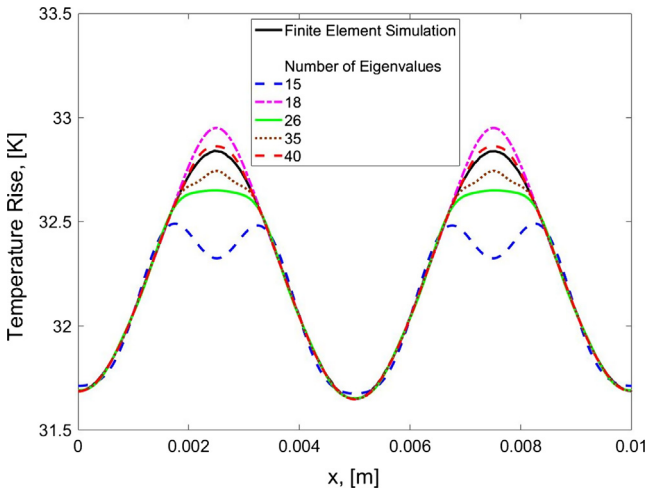

Fig. 5. Predicted temperature as a function of x for multiple number of eigenvalues, showing eventual convergence of the temperature distribution.

the number of eigenvalues increase. For this specific problem, Fig. 5 shows that around 40 eigenvalues are needed in each spatial direction for reasonable accuracy of better than 0.5%. For

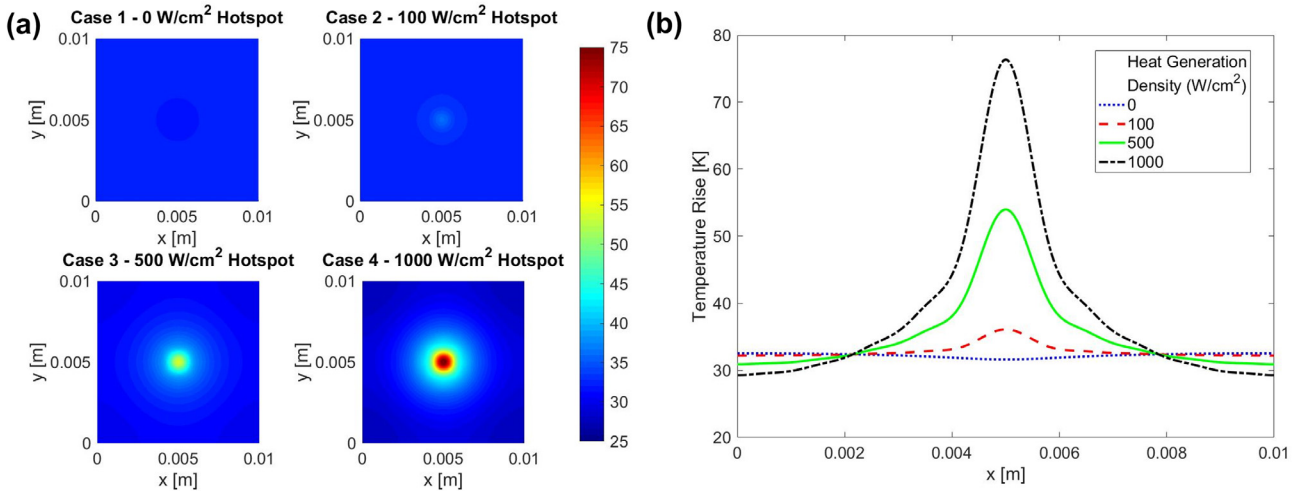

Fig. 6. Effect of localization of heat generation, demonstrated through four cases with equal total heat generation, but with increasingly denser heat generation in a hotspot. Cases 1 through 4 correspond to 0 W/m^2, 100 W/m^2, 500 W/m^2 and 1000 W/m^2 heat generation in a 1 mm by 1 mm hotspot at the center of the chip. The background heat generation in the rest of the chip is changed to maintain 10 W total heat generation in each case. (a) presents colorplots of temperature for each case, while (b) presents a lineplot of temperature as a function of x along the centerline of the die for each case.

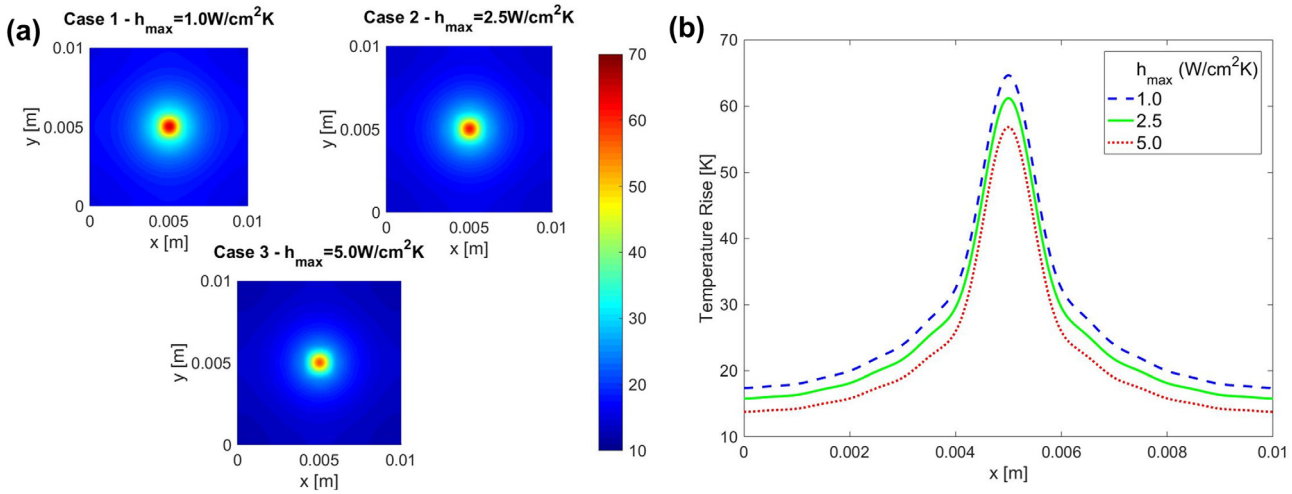

Fig. 7. Effect of changing the peak heat transfer coefficient of the impinging jet for the case of a single jet impinging upon a chip with a single hotspot at the center. (a) presents colorplots of temperature in each case, while (b) presents a lineplot of temperature as a function of x along the centerline of the die for each case.

a three-dimensional microprocessor, this corresponds to around 1681 unknown coefficients to determine, which is still not particularly challenging, since robust methods for solving much larger sets of algebraic equations exist and are commonly used.

The analytical model is then used for addressing a number of thermal optimization problems related to jet impingement cooling of a microprocessor. Fig. 6 shows the computed temperature distribution for a number of cases with the same power, but increasing heat generation density in a single hotspot located at the center of the microprocessor, which is being cooled by a jet impinging on the backside, along at the center of microprocessor. In each case, the background heat generation in the remainder of the chip is changed in order to maintain the total power dissipation in the chip. Colorplots in Fig. 6(a) for four cases of 0, 100, 500 and 1000 W/cm^2 dissipation in the hotspot show that as more and more heat is dissipated in a small region of the chip, the peak temperature rise increases significantly. This is also shown in Fig. 6(b) where the temperature rise is plotted along the centerline of the chip on the heat-generating face for the four cases. For a single 1000 W/cm^2 hotspot in the center, Fig. 7 presents the effect of changing h_{max}. As expected, increasing the value of h_{max} results in lower peak temperatures.

Fig. 8 examines the effect of varying the jet diameter on temperature distribution in the case of a single hotspot at the center of the chip. The jet also impinges at the center of the chip on the back face. Colorplots in Fig. 8(a) show minimal effect of increasing the jet diameter on peak temperature in the chip. This is also shown in the lineplots in Fig. 8(b) that show less than 5.3% change in peak temperature rise in changing the jet diameter from 0.1 mm to 1.0 mm. This may be a useful insight in the design of jet impingement cooling, since a lower diameter jet will consume much lesser cooling fluid without a dramatic impact on peak temperature.

The effect of the location of the jet is examined next. Fig. 9 presents computed temperature fields for a single hostpot in the center of the die being cooled by a single jet. Four cases with varying location of the jet impingement are computed. In case 1, the jet impingement corresponds to the center of the hotspot. In other cases, the jet progressively moves farther away from the center

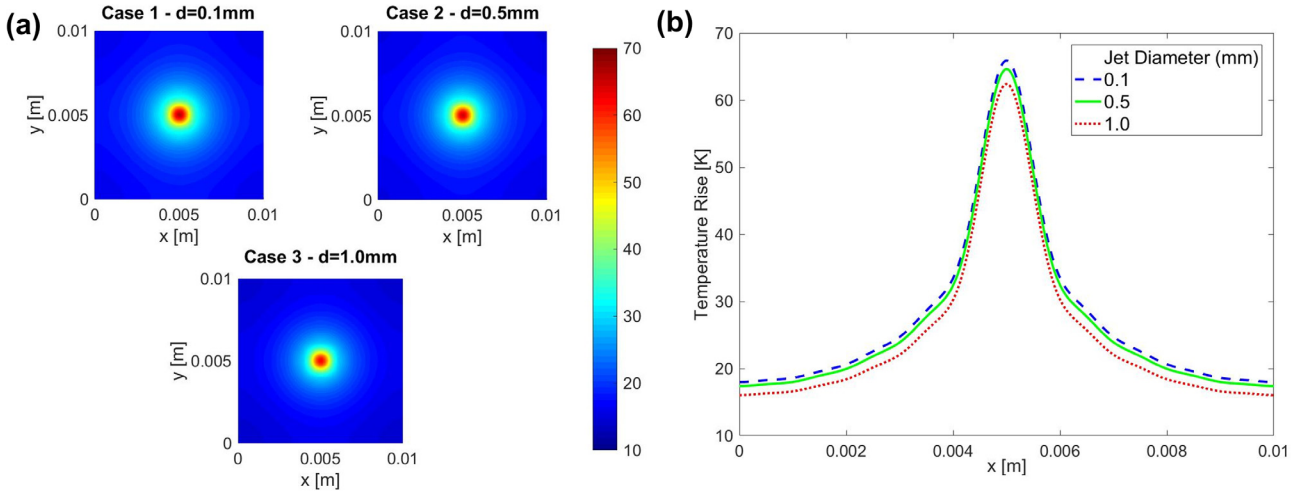

Fig. 8. Effect of jet diameter on cooling effectiveness, shown through three different convective heat transfer coefficient parameters for the same heat-generating chip. (a) shows colorplot of temperature for each case, while (b) shows lineplot of temperature as a function of x along the centerline of the die for each case.

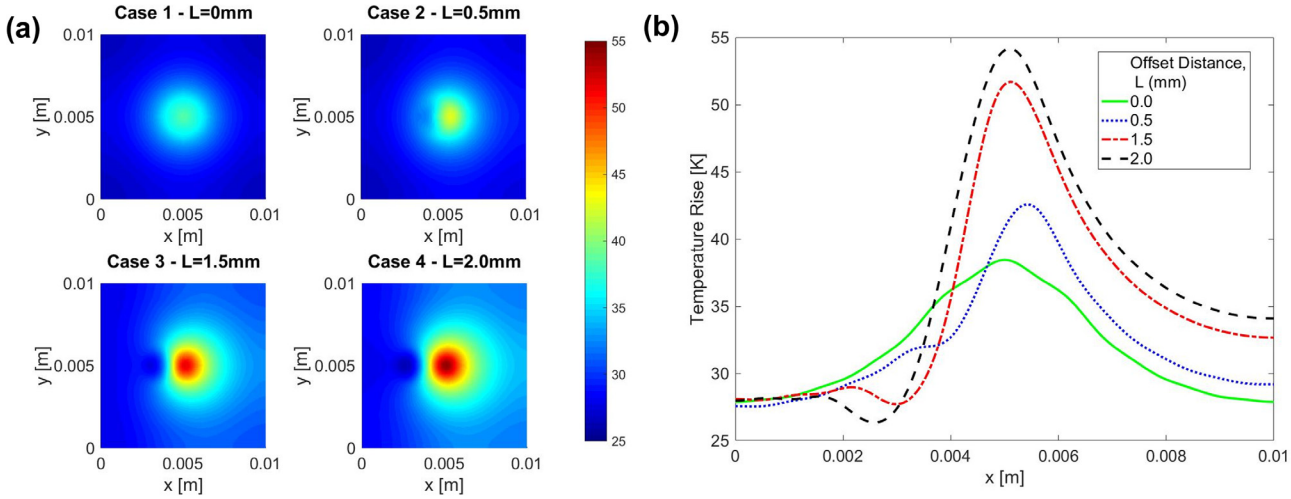

Fig. 9. Effect of changing the jet impingement location relative to the center of the hotspot, for cases with the distance between the two varying from 0 mm to 2 mm. (a) shows colorplot of temperature for each case, while (b) shows lineplot of temperature as a function of x along the centerline of the die for each case.

of the hotspot, thereby increasing the offset distance. As shown in the colorplots in Fig. 9(a) and lineplots in Fig. 9(b), Case 1 results in the lowest temperature as expected due to the alignment of heat dissipation with the cooling jet. Peak temperature rise in the chip becomes progressively larger as the jet moves farther away from the center of the hotspot. For Cases 2 through 4, the temperature plot in Fig. 9(b) shows a local depression in the temperature field at the location where the jet impinges on the chip.

Most modern microprocessor chips contain multiple computation and data storage blocks, each of which has its own power dissipation characteristics. The discrete power dissipation in each block is usually modeled through electrical simulations [28], and measured through voltage and current measurements. In general, the power map is significantly distributed due to the presence of multiple computation and data storage blocks, each of which dissipates power at different rates [29]. In case the chip is being cooled by multiple jets with different coolant flowrates, the variation of the convective heat transfer coefficient in space can also be complicated. In order to demonstrate the efficacy of the analytical model in such complicated scenarios, the temperature is computed when there are ten blocks of unequal sizes and heat dissipation rates on the chip, along with ten cooling jets of different characteristics and at different locations. In such a case, the resulting temperature field is not intuitive at all, and must be computed carefully in order to account for the effects of various parameters. Fig. 10 presents the heat dissipation map, variation of the convection heat transfer coefficient in space, and the resulting temperature field computed by the analytical model. As expected, the temperature field is quite complicated and not intuitive. For example, the peak temperature shown in Fig. 10(c) does not correspond to the block with the highest power. This happens because of the relatively small size of the block, which increases the power density, and because that block is not being effectively cooled by any of the cooling jets. Such quantification enabled by the analytical model is critical for a variety of optimization tasks, such as power distribution, distribution of cooling jets, as well as the allocation of coolant flow among the jets.

The analytical models presented here can also be used for optimization of transient thermal performance of jet-cooled microprocessors. An illustration is provided through a scenario summarized in Fig. 11. Here, two hotspots of equal strength 5 W/cm and size 1 mm are centered at 2.5 mm and 7.5 mm respectively. The first hotspot is active from $t = 0$ s to $t = 0.1$ s, whereas the second hot-

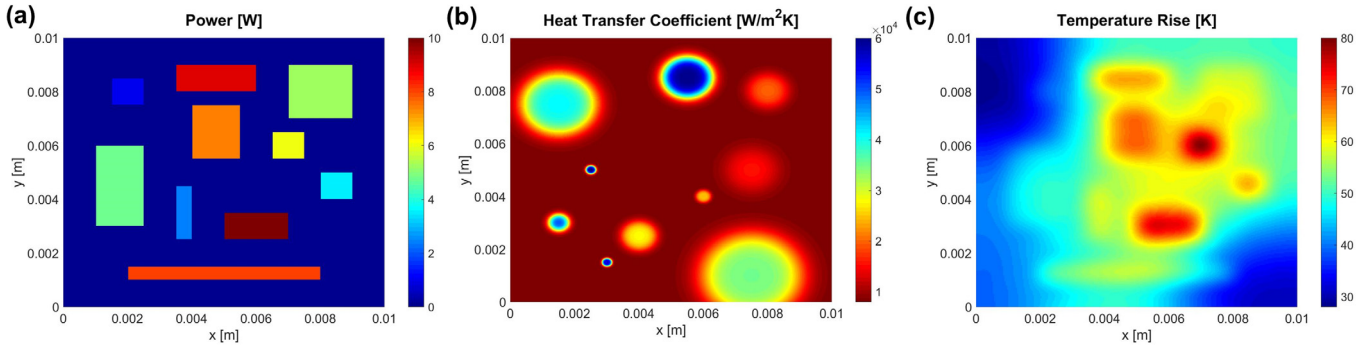

Fig. 10. (a) Power dissipation map, (b) Heat transfer coefficient distribution, and (c) resulting temperature field due to a complicated power map comprising ten heat dissipation regions with varying shapes and powers being cooled by ten impinging jets with varying locations and strengths.

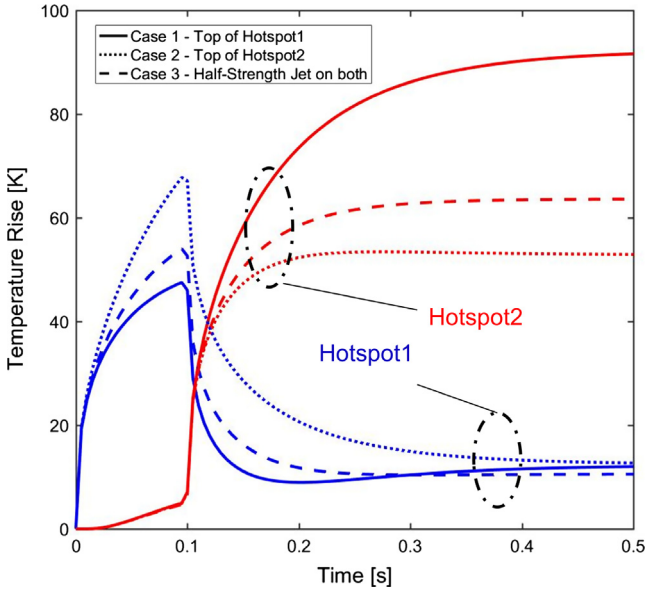

Fig. 11. Temperature as a function of time for a transient process involving two hotspots of equal magnitude, one of which is active between t = 0 s and t = 0.1 s and the other is active afterwards. Three cases shown include Cases 1 and 2 where a single jet is located directly under the first or second hotspot, while Case 3 has two half-strength jets on top of each hotspot.

spot becomes active at $t = 0.1$ s and remains active afterwards. Three jet configurations are considered. In the first case, the jet is located directly at the first hotspot, in which case, Fig. 11 shows reduced peak temperature of the first hotspot compared to the other two cases. However, due to the absence of direct cooling of the second hotspot, temperature of the second hotspot is significantly greater than the other two cases. These findings are reversed for Case 2, where a single jet impinges on top of the second hotspot. A compromise between these two extremes is shown in Case 3, where two equal strength jets impinge on each of the hotspots, due to which both hotspot temperatures are relatively lower and are between the extremes observed in Cases 1 and 2. Note that the strength of the two jets in Case 3 are determined assuming the same total coolant flowrate as Cases 1 and 2. Because the jet is most effective close to where it impinges, the splitting up of a single large jet into multiple smaller jets offers better thermal performance and ability to cool more hotspots.

While the choice of which cooling configuration to use depends on the overall thermal management objective, the analytical model presented here provides the capability for rapid computation of temperature rise due to a variety of thermal dissipation and spatially varying convective cooling of the microprocessor chip.

5. Conclusions

The cooling of microprocessor chips is a significantly important technological problem. Since heat dissipation in multicore microprocessor chips is highly distributed and dynamic, the localized cooling offered by jet impingement is very attractive. The analytical models presented here offer a robust technique for rapid computation of steady state and transient temperature rise in a microprocessor chip with spatially varying heat dissipation and convective cooling due to an impinging jet. The model has been validated against finite-element simulations and has been shown to be effective for analysis of a variety of optimization problems that may be encountered in jet impingement based thermal management design.

A key limitation of the model presented here is that it does not account for time-varying convective cooling. This could arise, for example, in an actively cooled chip where the location of the jet can be modulated in time. Development of a model for such a scenario is considerably complicated and is an important direction for future work.

References

[1] S.V. Garimella, Y.K. Joshi, A. Bar-Cohen, R. Mahajan, K.C. Toh, V.P. Carey, M. Baelmans, J. Lohan, B. Sammakia, F. Andros, Thermal challenges in next generation electronic systems-summary of panel presentations and discussions, IEEE Trans. Compon. Packaging Technol. 25 (2002) 69–575.
[2] J. Cho, K.E. Goodson, Thermal transport: cool electronics, Nat. Mater. 14 (2015) 136–137.
[3] S.G. Kandlikar, High flux heat removal with microchannels—a roadmap of challenges and opportunities, Heat Transfer Eng. 26 (2005) 5–14.
[4] A. Majumdar, Thermoelectric devices: helping chips to keep their cool, Nat. Nanotechnol. 4 (2009) 214–215.
[5] S.M. Sze, K.K. Ng, Physics of Semiconductor Devices, John Wiley & Sons, 2006.
[6] R. Mahajan, C. Chiu, G. Chrysler, Cooling a microprocessor chip, Proc. IEEE 94 (2006) 1476–1486.
[7] S. Khandekar, N. Dollinger, M. Groll, Understanding operational regimes of closed loop pulsating heat pipes: an experimental study, Appl. Therm. Eng. 23 (2003) 707–719.
[8] J.-Y. Chang, R. Prasher, S. Prstic, P. Cheng, H.B. Ma, Evaporative thermal performance of vapor chambers under nonuniform heating conditions, J. Heat Transfer 130 (2008) 121501.
[9] R.C. Chu, R.E. Simons, M.J. Ellsworth, R.R. Schmidt, V. Cozzolino, Review of cooling technologies for computer products, IEEE Trans. Device Mater. Rel. 4 (2004) 568–585.
[10] E.N. Wang, L. Zhang, L. Jiang, J.M. Koo, J.G. Maveety, E.A. Sanchez, K.E. Goodson, T.W. Kenny, Micromachined jets for liquid impingement cooling of VLSI chips, J. Microelectromech. Syst. 13 (2004) 833–842.
[11] J.-T. Cheng, C.-L. Chen, Active thermal management of on-chip hot spots using EWOD-driven droplet microfluidics, Exp. Fluids 49 (2010) 1349–1357.
[12] D. Kercher, J.-B. Lee, O. Brand, A. Glezer, Microjet cooling devices for thermal management of electronics, IEEE Trans. Compon. Packaging Technol. 26 (2003) 359–366.
[13] Y. Won, E.N. Wang, K.E. Goodson, T.W. Kenny, 3-D visualization of flow in microscale jet impingement systems, Int. J. Therm. Sci. 50 (2011) 325–331.

[14] C.T. Nguyen, N. Galanis, G. Polidori, S. Fohanno, C.V. Popa, A. Le Bechec, An experimental study of a confined and submerged impinging jet heat transfer using Al_2O_3-water nanofluid, Int. J. Therm. Sci. 48 (2009) 401–411.
[15] P. Tie, Q. Li, Y. Xuan, Heat transfer performance of Cu–water nanofluids in the jet arrays impingement cooling system, Int. J. Therm. Sci. 77 (2014) 199–205.
[16] B.W. Webb, C.F. Ma, Single-phase liquid jet impingement heat transfer, Adv. Heat Transfer 26 (1995) 105–217.
[17] X. Liu, J.H. Lienhard, J.S. Lombara, Convective heat transfer by impingement of circular liquid jets, J. Heat Transfer 113 (1991) 571–582.
[18] L. Choobineh, A. Jain, Analytical solution for steady-state and transient temperature fields in vertically stacked 3-D integrated circuits, IEEE Trans. Components Packaging & Manufac. Technol. 2 (2012) 2031–2039.
[19] S.W. Ma, A.I. Behbahani, Y.G. Tsuei, Two-dimensional rectangular fin with variable heat transfer coefficient, Int. J. Heat Mass Transfer 34 (1991) 79–85.
[20] D. Sarkar, A. Jain, R.J. Goldstein, V. Srinivasan, Corrections for lateral conduction error in steady state heat transfer measurements, Int. J. Therm. Sci. 109 (2016) 413–423.
[21] D. Sarkar, K. Shah, A. Haji-Sheikh, A. Jain, Analytical modeling of temperature distribution in an anisotropic cylinder with circumferentially-varying convective heat transfer, Int. J. Heat Mass Transfer 79 (2014) 1027–1033.
[22] D. Sarkar, A. Haji-Sheikh, A. Jain, Thermal conduction in an orthotropic sphere with circumferentially varying convection heat transfer, Int. J. Heat Mass Transfer 96 (2016) 406–412.
[23] H.S. Carslaw, J.C. Jaeger, Conduction of Heat in Solids, 2nd ed., Clarendon Press, Oxford, 1959.
[24] R.V. Churchill, Fourier Series and Boundary Value Problems, McGraw Hill, 1941.
[25] M.N. Özışık, Heat Conduction, John Wiley & Sons, 1993.
[26] F.R. de Hoog, J.H. Knight, A.N. Stokes, An improved method for numerical inversion of Laplace transforms, S.I.A.M. J. Sci. Stat. Comput. 3 (1982) 357–366.
[27] K.J. Hollenbeck, INVLAP.M: A matlab function for numerical inversion of Laplace transforms by the de Hoog algorithm. (1998) Available at: <http://www.mathworks.com/matlabcentral/answers/uploaded_files/1034/invlap.m> (Accessed: January 1, 2016).
[28] A. Paul, S.P. Park, D. Somasekhar, Y.M. Kim, N. Borkar, U.R. Karpuzcu, C.H. Kim, System-level power analysis of a multicore multipower domain processor with on-chip voltage regulators, IEEE. Trans. VLSI 24 (2016) 3468–3476.
[29] H.F. Hamann, A. Weger, J.A. Lacey, Z. Hu, P. Bose, E. Cohen, J. Wakil, Hotspot-limited microprocessors: direct temperature and power distribution measurements, IEEE J. Solid-State Circuits 42 (2007) 56–65.